Measurement and Simulation of the Neutron Travel Time Distribution inside a Neutron Monitor

K. Chaiwongkhot,[a,*] **D. Ruffolo,**[a] **W. Yamwong,**[b] **J. Prabket,**[b] **P.-S. Mangeard,**[c] **A. Sáiz,**[a] **W. Mitthumsiri,**[a] **C. Banglieng,**[d] **E. Kittiya,**[e] **W. Nuntiyakul,**[e] **U. Tippawan,**[e] **M. Jitpukdee**[f] **and S. Aukkaravittayapun**[g]

[a]*Department of Physics, Faculty of Science, Mahidol University, Bangkok, Thailand*

[b]*Thai Microelectronics Center (TMEC), National Electronics and Computer Technology Center (NECTEC), Chachoengsao, Thailand*

[c]*Bartol Research Institute and Department of Physics and Astronomy, University of Delaware Institution, Newark, Delaware, USA*

[d]*Division of Physics, Faculty of Science and Technology, Rajamangala University of Technology Thanyaburi, Pathum Thani, Thailand*

[e]*Department of Physics and Materials Science, Faculty of Science, Chiang Mai University, Chiang Mai, Thailand*

[f]*Department of Applied Radiation and Isotopes, Faculty of Science, Kasetsart University, Bangkok, Thailand*

[g]*National Astronomical Research Institute of Thailand (NARIT), Chiang Mai, Thailand*

E-mail: pha.hikari@gmail.com

Using a setup for testing a prototype for a satellite-borne cosmic-ray ion detector, we have operated a stack of scintillator and silicon detectors on top of the Princess Sirindhorn Neutron Monitor (PSNM), an 18-counter NM64 detector at 2560-m altitude at Doi Inthanon, Thailand. Monte Carlo simulations have indicated that about 15% of the neutron counts by PSNM are due to interactions (mostly in the lead producer) of GeV-range protons among the atmospheric secondary particles from cosmic ray showers, which can be detected by the scintillator and silicon detectors. Detection of incoming charged particles associated with neutron counts in the NM64 allows a measurement of the travel time distribution of such neutrons as they scatter and propagate through the NM64, processes that are nearly the same whether the interaction was initiated by an energetic proton (for 15% of the count rate) or neutron (for 80% of the count rate). This travel time distribution underlies the time delay distribution between successive neutron counts, from which we can determine the leader fraction (inverse multiplicity), which has been used to monitor Galactic cosmic ray spectral variations over ~1-40 GV. In the present experiment we have measured both the coincidence rate of incident charged shower particles with neutron counts in the NM64 and the neutron travel time distribution. We utilize these measurements to validate Monte Carlo simulations of atmospheric secondary particle detection by the NM64 and the resulting yield functions used to interpret the count rate and the leader fraction.

*** 37th International Cosmic Ray Conference (ICRC2021), ***
*** 12-23 July 2021 ***
*** Berlin, Germany - Online ***

---

*Presenter

1. Introduction

Cosmic ray particles can be detected either directly in space, or indirectly by means of air showers generated by their interactions in Earth's atmosphere, e.g., using ground-based detectors. A neutron monitor (NM) detects atmospheric secondary particles (mostly neutrons) produced by GeV-range primary cosmic ray ions [1]. The neutron time delay is the time difference between successive neutron detection times, which are sampled from the more fundamental distribution of the travel time between the arrival of an atmospheric secondary particle at the monitor and the detection of a neutron [2, 3]. From the time delay distribution, one can determine the leader fraction L, i.e., the fraction of neutron counts that did not follow another count from the same primary cosmic ray [4]. Quantitative interpretation of changes in the leader fraction in terms of changes in the cosmic ray spectral index relies on results from Monte Carlo simulations (see Appendix E of [5]).

In the present work, we have performed an experiment with two objectives: 1) to test prototype detector components for a satellite-borne cosmic-ray ion detector, and 2) to use the measurement of charged particles entering a neutron monitor to study the neutron travel time distribution inside an NM and validate Monte Carlo calculations. Here we report on the second objective, to study the neutron travel time distribution and compare between experimental and simulation results. While most NM counts are due to atmospheric secondary neutrons, GeV-range secondary protons account for 15% of the PSNM count rate [6] and provide the dominant contribution among charged secondary particles. Indeed, after secondary particles interact inside the NM (typically in the lead producer) to produce neutrons, the scattering and propagation of such neutrons should be similar whether the interaction was initiated by an energetic proton or neutron. Thus we can perform non-destructive measurement of charged secondary particles, based on their ionization of a detector medium as they pass through, to provide a timing signal for measurement of the neutron travel time.

2. Experimental Methods

Figure 1(a) shows the setup of this experiment. An array of PIN silicon detectors, fabricated as a prototype for a satellite-borne cosmic-ray ion detector, and a commercial scintillator were covered in black cloth and placed over the PSNM, as schematically indicated in Figure 1(b).

PSNM is a neutron monitor of the NM64 design [7]. It contains 29 tons of lead producer (Pb), in which a cosmic-ray-generated atmospheric secondary particle (usually a neutron, but also possibly a charged particle) can disrupt a lead nucleus to produce several neutrons. The NM64 uses polyethylene (PE) to moderate and reflect such neutrons. PSNM employs 18 BP-28 neutron-sensitive proportional counters (PC) (Chalk River Laboratories, Canada). Neutrons can be detected by means of the reaction $n(^{10}B, ^7Li)^4He$.

PSNM is located at the summit of Doi Inthanon, Thailand's highest mountain, at geographic coordinates 18.59°N, 98.49°E, at an altitude of about 2560 m above sea level. Near Earth's magnetic equator, it has the world's highest vertical cutoff rigidity for a fixed station, 16.7 GV. For more details about this specific monitor, see [4].

The plastic scintillator (Epic Crystal, China) with the dimensions of 60 mm × 80 mm × 5 mm, together with the array of PIN silicon detectors, were set up on top of PSNM to detect ionization

in the material due to the passage of charged atmospheric secondary particles entering the neutron monitor. The scintillation light was readout by a silicon photomultiplier (SiPM; ASD-NUV4S-P and ASD-EP-EB-PZ, AdvanSiD, Italy).

The array of PIN silicon detectors, as well as preamplifiers and a merging amplifier, were fabricated at the Thai Microelectronics Center (TMEC). The PIN array prototype detector had some noise problems, so for the purpose of measuring the neutron travel time distribution inside PSNM, we have used the scintillator signal to provide a timing trigger indicating the passage of a charged atmospheric secondary particle from a cosmic ray shower. In this experiment, the PIN array and scintillator were positioned directly over the wire of PSNM's Tube 1, an end counter, as indicated in Figure 1(b). An oscilloscope (DS1104Z Plus, Rigol, China) was used to record data from the scintillator, PIN array, and PSNM Tube 1 (amplifier waveform) from 0.5 ms before to 5.5 ms after a scintillator trigger, with 30,000 sampling points at 200 ns cadence per detection channel. The data were transferred directly from the oscilloscope to the back-end computer. The transfer time caused a dead time of around 1.7 s for each scintillator trigger event.

Data were taken over two time periods in February, 2021: 1) from February 22 at 10:54 UT to February 25 at 08:16 UT, and 2) from February 26 at 02:59 UT to February 27 at 00:42 UT. Later, the output waveform
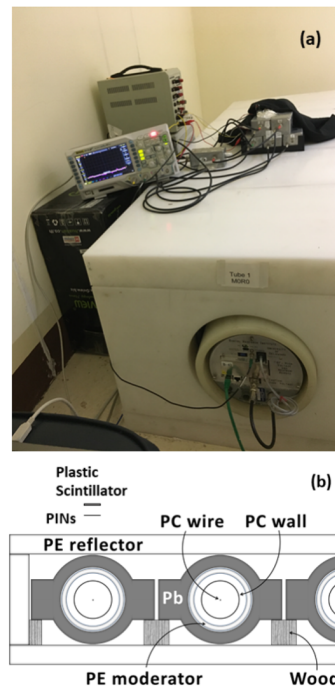

Figure 1: (a) Experimental setup, with charged particle detectors (scintillator and Si PIN array) covered by a black cloth and placed on top of the Princess Sirindhorn Neutron Monitor at the summit of Doi Inthanon, Thailand. (b) Schematic cross-section of the detector configuration.

from PSNM Tube 1's shaping amplifier was analyzed in terms of NM pulses in post-analysis. In the present work, distributions of the NM pulses in time, relative to the charged-particle trigger, and in pulse height are discussed in detail in Section 4.

3. Monte Carlo Simulations

For the purpose of this analysis we upgraded our simulation previously used in [6, 8] to be compatible with the recent version 4-1.1 of Fluka [9, 10]. Layers of plastic scintillator and silicon detectors were added to the geometry of the PSNM station to reflect the experimental configuration.

We simulated the interaction of the three most important types of charged secondary particles (protons and negative and positive muons) at ground level with the 18NM64. The simulated particles were injected downward from 10 μm above the scintillator. Their flux and spectrum were set according to output from EXPACS 4.09 [11] for the altitude, latitude, and longitude of PSNM, under solar minimum conditions as appropriate for the time of our experiment. To avoid problems of limited statistics for high energies, our simulations used 1 million proton and 1 million muon events. Muons were simulated from 10 MeV to 25.12 GeV and the protons were simulated from 631 MeV to 19.95 GeV. The zenith angle (θ) dependence of the flux was also taken into account for

$0.625 \le \cos\theta \le 1$. The most horizontal incoming particles at $\cos\theta < 0.625$ are expected to have a small contribution and were not simulated.

4. Results

4.1 Overview of Travel Time Distribution

Timing and pulse height data PSNM Tube 1 were analyzed for time intervals from -0.5 to 5.5 ms relative to 165,500 charged particle triggers, which were found to contain 35,661 NM pulses. The distribution in pulse height and time is shown in Figure 2. There is a uniform "background" distribution at all times, which we attribute to chance coincidences of NM pulses unrelated to the passage of the charged particle.

Indeed, most NM pulses can be attributed to atmospheric secondary neutrons, rather than charged particles, from cosmic ray showers, and they could result from atmospheric secondaries incident over a much wider area than the 6×8 cm^2 scintillator. Nevertheless, we do observe a significant increase in the NM pulse distribution shortly after the charged-particle trigger, for $0 \le t \le 1.5$ ms. We interpret the excess pulse rate, over the uniform background from chance coincidences, as the travel time distribution for NM pulses associated with a charged particle entering the NM64 detector. Pulses due to neutron-induced fission will hereafter be referred to as "neutron" pulses. This standard pulse height distribution includes "wall-effect" neutron pulses, lost due to colliding with the wall of the counter, at lower pulse heights.

During background times, there was a uniform distribution of pulses at low pulse height, $PH < 1$ V, which is consistent with wall-effect neutron pulses. In addition, Figure 2(b) shows that within 20 µs after the trigger, there was a strong enhancement of pulses at low pulse height, with a much higher density relative to the main neutron peak than during background times before the trigger, es-
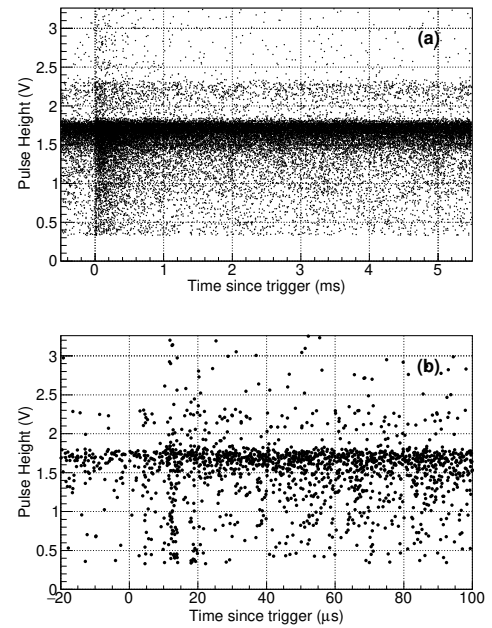

Figure 2: Scatter plots of pulse height PH vs. time t relative to a charged-particle trigger for each pulse in PSNM Tube 1, a neutron-sensitive proportional counter (PC), (a) for all data ($-0.5 \le t < 5.5$ ms) and (b) for $-20 \le t < 100$ µs.

pecially at $PH < 1$ V. We attribute this enhancement to ionization in the PC due to passage of energetic charged particles.

In Figure 3 neutron pulses are identified from neutron-induced fission of ^{10}B in the proportional counter. Simulated pulses are all neutron pulses, with the exception of the spike at $t = 0$ in panel (d), which is mainly due to charged-particle ionization. Note that the experimental distributions include a uniform background due to NM pulses unrelated to the charged-particle trigger, which are not included in the simulation. The experimental and simulated distributions are in good agreement, except that the experimental distribution (a) shows a spike of promptly detected neutrons at $0 \le t < 20$ µs that is not present in the simulated distribution (c).
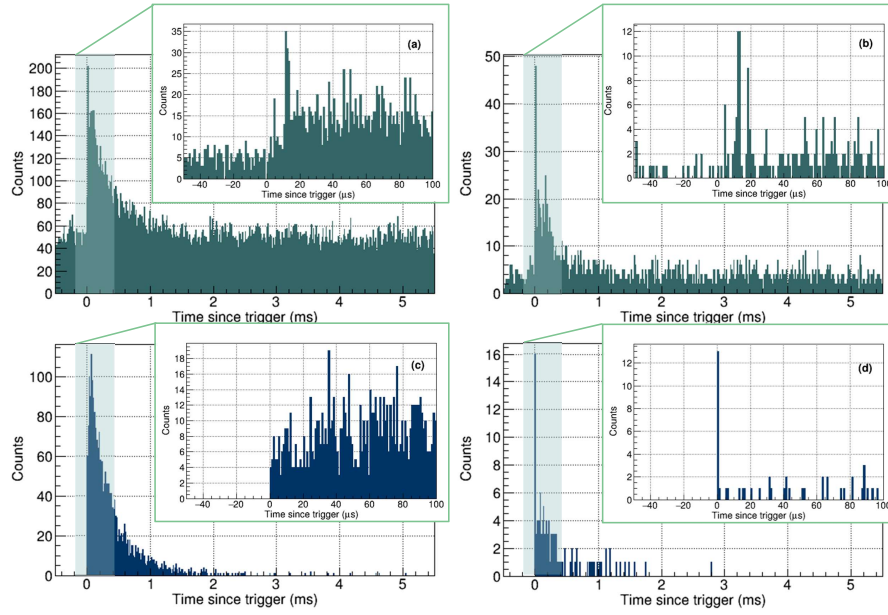
Figure 3: Distribution in time t (relative to a charged-particle trigger) of pulses in PSNM Tube 1 with $-0.5 \leq t < 5.5$ ms and the insertion of the same distribution with $-50 \leq t < 100$ μs for (a) high pulse height, $PH \geq 1$ V, from neutron pulses and (b) low pulse height, $0.326 \leq PH < 1$ V, representing wall-effect neutron pulses and charged-particle ionization, as well as Monte Carlo simulation results for energy deposition ranges corresponding to (c) high pulse height and (d) low pulse height.

The insert to each panel of Figure 3 shows the same distribution but for $-50 \leq t < 100$ μs. During $0 \leq t < 20$ μs, there is an enhanced rate of promptly detected neutron pulses at high pulse height in the experiment (a) but not for the simulation (c). The experimental timing has a delay of $\approx 10 \pm 10$ μs, so these are consistent with $t = 0$. At low pulse height, the pulse is much more prominent, and the simulated pulses (d) during the spike at $t = 0$ are mostly due to charged-particle ionization and at later times entirely wall-effect neutron pulses; this interpretation can be applied to the experimental results (b) during $0 \leq t < 20$ μs and $t \geq 20$ μs, respectively.

4.2 Prompt NM Pulses and Multiplicity

Figure 4 shows results from the Monte Carlo simulation for the distribution of neutron capture events as a function of the neutron kinetic energy when captured, E, and the time of the capture event, t. Most capture events are for thermal
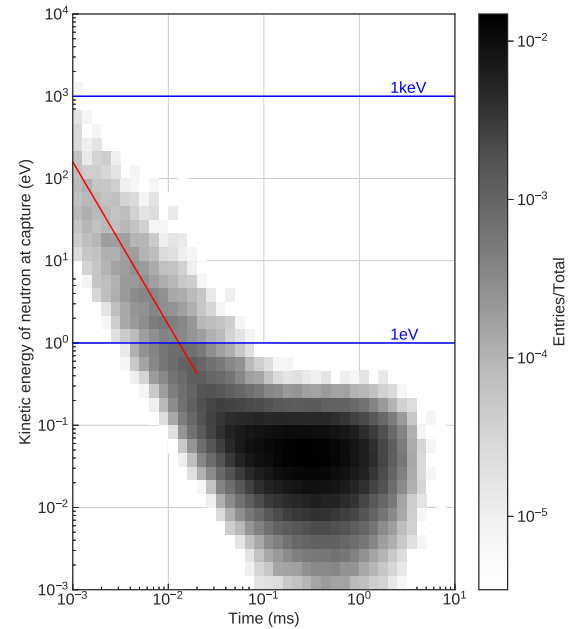

Figure 4: Simulated distribution of neutron capture events as a function of kinetic energy of the neutron when captured and time of capture relative to charged-particle injection just above the scintillator.

neutrons, i.e., for events with a kinetic energy at capture within an order of magnitude of the thermal energy at room temperature of about 0.025 eV. Thermal neutron capture times are seen to range from ~20 μs to 3 ms. A best-fit power-law for that extension has a slope of −2.0 (see Figure 4), corresponding to $E \propto t^{-2}$. In terms of the neutron velocity at capture, this can be expressed as $v = s/t$ for $s = 18$ cm, which can be interpreted as a characteristic distance such that t is the time of flight at speed v over the distance s.

We have found another special characteristic of the promptly detected NM pulses, regarding the multiplicity of pulses, i.e., the number of pulses recorded in one time sample. Figure 5 presents the multiplicity during two different time periods, from 1.5 to 5.5 ms and from 0 to 1.5 ms. In Figure 5(a), we examine pulses that occur between 1.5 to 5.5 ms, which is significantly later than a charged-particle trigger, and are therefore mostly unrelated to that charged particle. It is seen that prompt pulses are frequently associated with events of unusually high multiplicity, e.g., from charged secondary particles of particularly high energy. The mean multiplicity is 1.44.

In Figure 5(b), we consider time periods from 0 to 1.5 ms after a charged-particle trigger, with at least one NM pulse. The resulting multiplicity distribution is quite similar except with a slightly higher relative occurrence rate of high multiplicity ($M \geq 4$), and a much higher relative occurrence of very high multiplicity ($M \geq 21$). Nevertheless, the mean multiplicity is similar, at 1.66.

Next, Figure 5(c) shows the multiplicity distribution for a subset of time periods from 0 to 1.5 ms in which there was at least one prompt pulse, with $0 \leq t < 20$ μs, at high pulse height $PH \geq 1$ V, indicating a prompt neutron detection. The mean multiplicity is 6.22, with a substantial fraction of time periods having a high multiplicity, up to $M = 62$. In fact, for the event with $M = 62$, the train of pulses extended to about 3.2 ms, well beyond the range of 1.5 ms included in Figure 5(b), and also had substantial pileup, so the actual multiplicity was much higher than that.

Finally, Figure 5(d) is like Figure 5(c), except for requiring at least one prompt pulse at low pulse height, $PH < 1$ V, usually indicating detection of a prompt charged-particle ionization signal. The frequency of high multiplicity periods is again greatly enhanced relative to background time periods, now with a mean multiplicity of 6.26. In this case the highest observed multiplicity was $M = 23$. This is lower than the maximum multiplicity seen in Figure 5(c); however, the mean multiplicities are similar and the distributions may be consistent, with a higher maximum in Figure 5(c) because of a larger sample. The reason for the high multiplicity of events containing at least one promptly detected pulse is not clear; they may relate to multiple secondary particles.

4.3 Diffusion-Absorption Model

We now consider whether the peak and tail parts of the travel time distribution can be explained by processes of neutron diffusion and absorption inside the NM. For simplicity, we propose an analytic model in which these processes are treated as spatially uniform: $\partial n/\partial t = D\nabla^2 n - \alpha n$
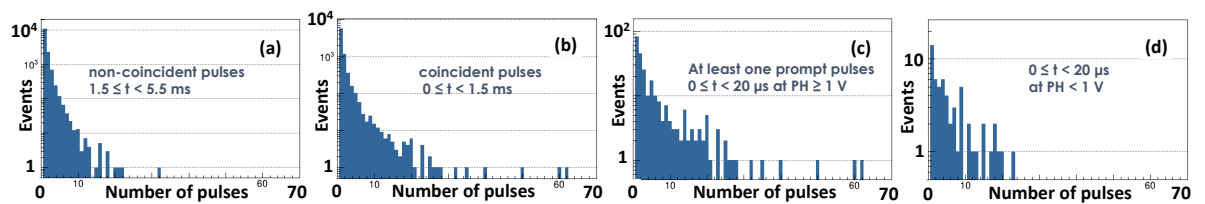

Figure 5: Multiplicity distributions of pulses in PSNM Tube 1 for various sets of time periods.

where n is the areal density of neutrons in terms of their projected (x, y) positions in the plane perpendicular to the axis of the proportional counters, and t is the time since entry of the atmospheric secondary particle. Here D is a neutron diffusion coefficient and α is the rate of neutron absorption by materials inside the NM64, including the capture by ^{10}B that results in detection. Spatial boundaries are neglected, i.e., the (x, y) domain is considered as infinite. For neutron production at $x = y = 0$, the solution is

$$
\begin{aligned}
n &\propto \frac{1}{t} \exp\left(-\frac{x^2 + y^2}{4Dt}\right) \exp(-\alpha t) \\
&\propto \frac{1}{t} \exp\left(-\frac{T_r}{t}\right) \exp(-\alpha t)
\end{aligned}
\tag{1}
$$

where for fitting purposes, x, y, and D can be combined into a single parameter, the rise time $T_r \equiv (x^2 + y^2)/(4D)$. Our equation is similar to, but simpler than, an equation used by [12] for neutron transport in nuclear reactors; however, to our knowledge such a model has not previously been used to describe the travel time distribution inside an NM.

Equation (1) was used to fit neutron travel time profiles for both experimental and Monte Carlo data, with fit parameters as T_r, α, an overall normalization N, and (for the case of experimental data) an added uniform background rate C due to chance coincidences. We use this equation to fit the peak and tail of the neutron travel time distributions during $0.02 \leq t < 5.5$ ms. We exclude promptly detected pulses (at $0 \leq t < 20$ μs) because those are partly due to charged-particle ionization and partly to neutrons of higher energy (see Figure 4) whose transport is not governed by diffusion and absorption.

The fitting results in Figure 6 indicate that the neutron diffusion-absorption model can describe the measured time profile very well. The best-fit parameters for the experimental neutron travel time distribution were the rise time $T_r = 0.063 \pm 0.004$ ms, absorption rate $\alpha = 0.57 \pm 0.11$ ms^{-1}, normalization constant $N = 24 \pm 1$ counts per bin, and background rate $C = 48.7 \pm 0.5$ counts per bin. The fit χ^2 per degree of freedom was 1.18, confirming a very good fit.

Figure 6 also shows the best-fit to the simulated neutron travel time distribution, for which $T_{r,MC} = 0.069 \pm 0.003$ ms, $\alpha_{MC} = 1.25 \pm 0.06$ ms^{-1}, and $N_{MC} = 21.1 \pm 0.9$ counts per bin, where the fit profile for simulated data has been multiplied by 1.3 to match the peak height of the experimental fit profile.

Figure 6: Experimental travel time distribution for all NM pulses over $-0.5 \leq t < 1.5$ ms, together with fits to experimental data (red band), experimental data subtracting a uniform background due to chance coincidences (blue band), and normalized simulation data (orange band) using a 2D neutron diffusion-absorption model (Equation 1).

5. Discussion and Conclusions

Using a setup for testing a prototype for a satellite-borne cosmic-ray ion detector placed on top of the PSNM can provide a timing trigger for measurement of the travel time distribution of
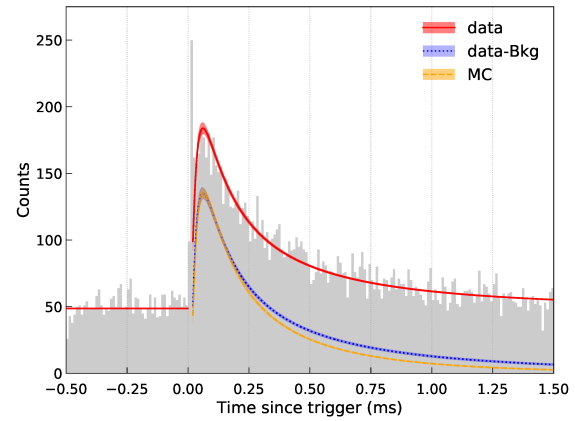
locally produced neutrons as they scatter and propagate through the NM64, processes that are similar whether the interaction was initiated by an energetic proton (for 15% of the count rate) or neutron (for 80% of the count rate). This travel time distribution underlies the time delay distribution between successive neutron counts, from which we can determine the leader fraction (inverse multiplicity).

Here we have measured and characterized the travel time distribution from both the experimental setup and Monte Carlo simulations of atmospheric secondary particle detection. We confirm a known travel time distribution with a peak (at ≈70 μs) and tail over a few ms, dominated by neutron counts. In addition we identify a group of prompt neutron monitor pulses that arrive within 20 μs of the charged-particle trigger, of which a substantial fraction can be attributed to charged-particle ionization in a proportional counter, according to both experimental and Monte Carlo results. Prompt pulses, either due to neutrons or charged-particle ionization, are associated with much higher mean multiplicity than typical pulses. These results validate and point the way to some improvements in Monte Carlo simulations and the resulting yield functions used to interpret the neutron monitor count rate and leader fraction. A full report on these results and discussion was presented by [13].

Acknowledgments

References

[1] J. A. Simpson *Physical Review*, vol. 73, June 1948.

[2] E. B. Hughes *et al. Proceedings of the Physical Society*, vol. 83, Feb. 1964.

[3] V. P. Antonova *et al. Journal of Physics G Nuclear Physics*, vol. 28, Feb. 2002.

[4] D. Ruffolo *et al. Astrophysical Journal*, vol. 817, Jan. 2016.

[5] C. Banglieng *et al. Astrophysical Journal*, vol. 890, Feb. 2020.

[6] N. Aiemsa-ad *et al. Journal of Geophysical Research (Space Physics)*, vol. 120, July 2015.

[7] C. J. Hatton and H. Carmichael *Canadian Journal of Physics*, vol. 42, Dec. 1964.

[8] P. S. Mangeard *et al. Journal of Geophysical Research (Space Physics)*, vol. 121, Aug. 2016.

[9] G. Battistoni *et al.*, "Overview of the fluka code," *Annals of Nuclear Energy*, vol. 82, 2015.

[10] T. Böhlen *et al. Nuclear Data Sheets*, vol. 120, 2014.

[11] T. Sato *PLOS ONE*, vol. 11, 08 2016.

[12] J. R. Lamarsh, *Introduction to Nuclear Reactor Theory*. Reading, MA: Addison-Wesley, 1966.

[13] K. Chaiwongkhot *et al. Astroparticle Physics*, vol. 132, 2021.